Persistence of a Subsurface Water Mass in a Deep Mid-Latitude Fjord

Laura Bianucci[1], Jennifer. M. Jackson[1,2], Susan E. Allen[2], Maxim Krassovski[1], and Ian J.W. Giesbrecht[3,4]

[1]Institute of Ocean Sciences, Fisheries and Oceans Canada, Sidney, BC, Canada
[2]The University of British Columbia, Vancouver, BC, Canada
5   [3]Hakai Institute, Vancouver, BC, Canada
[4]Simon Fraser University, Vancouver, BC, Canada

Correspondence to: Laura Bianucci (laura.bianucci@dfo-mpo.gc.ca)

Abstract.

Fjords are common geomorphological coastal features in the mid- and high-latitudes, carved by glacial erosion. These deep
10   nearshore zones connect watersheds and oceans, typically behaving as an estuary. Many fjords in the world have shown
concerning warming and deoxygenation trends in their deep waters, sometimes at faster rates than the open ocean. While that
is the case in several fjords of British Columbia (BC), Canada, some of the same fjords have shown that strong Arctic outflow
wind events in winter can lead to cooling and reoxygenation of subsurface waters, with effects lasting until the following
autumn. The latter was observed in Bute Inlet, BC in 2019. We used a high-resolution, three-dimensional ocean model to
15   investigate the mechanisms allowing for the persistence of these subsurface conditions through the year. The presence of the
subsurface cold water mass reduced the already weak residual circulation, changing its vertical structure from three to four
layers. The reduction of mixing and advection allowed for the water mass to stay in place until autumn conditions arrived (i.e.,
strong wind mixing and reduced freshwater forcing). The identification of mechanisms that allow for the persistence of cold
and oxygenated conditions are key to understand potential areas of ecological refugia in a warming and deoxygenating ocean.

20   **1 Introduction**

High- and mid-latitude coastlines are beset with innumerable fjords, remnants of glacial periods. The importance of these
coastal geomorphological features extend to many realms, since they provide habitats for multiple species (Arimitsu et al.,
2012; Keen et al., 2017; Mathews and Pendleton, 2006; Frid et al., 2021), receive inputs from both the watersheds and the
neighbouring ocean (Bianchi et al., 2020; St. Pierre et al., 2022), and offer protected waters for transportation, aquaculture,
25   fisheries, and other human activities (Iriarte et al., 2010; Bergh et al., 2023). They are also important sites for traditional
cultures (e.g., Ball, 2021; Brattland, 2010). Global organic carbon burial rates in fjords are disproportionately large for their
small area size (Smith et al., 2015) and their high sedimentation rates allow for high-resolution records of past climates (Bianchi
et al., 2020). Fjords properties have been changing in the last several decades showing, for instance, evidence of warming and
deoxygenation in several parts of the world (Aksnes et al., 2019; Jackson et al., 2021; Linford et al., 2023). While further
30   changes are to be expected in the future, it is still uncertain how climate change will affect current fjord ecosystems.

One of the fjords showing long-term trends is Bute Inlet (Jackson et al., 2021), a mainland fjord in British Columbia (BC, Canada; Fig. 1b) that lies within the traditional territory of the Homalco First Nation. It is about 80 km long and 3 km wide, with a maximum depth of 730 m and a single 355 m sill at its mouth (Pickard, 1961). Approximately 94% of the freshwater entering Bute Inlet is supplied by two major rivers near the head (Homathko and Southgate, Fig. 1a) while the rest of the freshwater is provided by small streams (Farrow et al., 1983). A recent study determined that about three times more terrestrial organic carbon per unit of surface area is buried in Bute Inlet sediments each year compared with other studied fjords (Hage et al., 2022), suggesting that this inlet is an important conduit for land-sea exchange as well as a region with high primary productivity. The high rates of terrestrial carbon burial are partly due to the frequent turbidity currents in Bute Inlet (Heijnen et al., 2020; Hage et al., 2022), which are associated with river discharge and tides (Bailey et al., 2023). Effects of climate change are already clear in Bute Inlet; for instance, its deep waters (i.e., below sill depth) warmed by 1.3°C and lost about 0.6 mL L^{-1} of oxygen from 1951 to 2020 (Jackson et al., 2021). Furthermore, a landslide in November 2020 caused by rapid deglaciation in a Southgate River tributary created a land-based tsunami and subsequent outburst flood; the generated sediment plume was observed in Bute Inlet more than 60 km from its source (Geertsema et al., 2022).

Despite the observed warming and deoxygenation at depth, recent observations in Bute Inlet showed that subsurface (i.e., above the sill depth) cold and oxygen-rich waters originated during an Arctic outflow wind event in February 2019 and persisted until the following fall (Jackson et al., 2023). Such subsurface temperature minima had been previously observed in BC fjords and suggested to be associated to Arctic outflow events (MacNeill, 1974; Pickard, 1961). The long permanence of such subsurface characteristics could alleviate deteriorating conditions and/or provide refugia to multiple species as climate changes (Ducklow et al., 2022; Jackson et al., 2023). How these winter-generated subsurface conditions can remain unchanged for almost a whole year has not yet been studied.

Here, we used a high-resolution three-dimensional numerical ocean model to investigate the mechanisms leading to the long persistence of the 2019 cold/oxygenated subsurface feature in Bute Inlet. We analyzed summer simulations with and without the subsurface cold feature, describing the along-fjord circulation under both conditions. In the discussion, we examine how the modelled multi-layer circulation in Bute Inlet compares to other deep fjords in the world, and how the subsurface feature is a new water mass that weakens the residual circulation, creating a barrier for mixing and advection. Thus, it is able to stay mostly in place until autumn conditions arrive (i.e., stronger winds and reduced freshwater forcing after peaking during the summer freshet).

2 Methods

2.1 Model grid, parameter values, and parameterizations

The model used for this work evolved from the Finite Volume Community Ocean Model (FVCOM; Chen et al., 2003, 2006) application for the Discovery Islands developed by Foreman et al. (2012), herein referred to as F12. For the present work, the FVCOM code was upgraded from version 2.7 to 4.1 (Chen et al., 2013). The grid was mostly the same as in F12 (horizontal

resolution from ~13 m in the narrowest channels to ~1 km at the Strait of Georgia boundary; resolution calculated as the square root of the element area), except for a refinement in Bute and Toba Inlets to improve the representation of the flow in those

65 deep, narrow, and steep-sided fjords. The model bathymetry in these inlets was regenerated using a 10-meter resolution digital elevation model (Government of Canada, 2021), and the model grid excluded the steepest sections of the near-shore while also increasing the resolution, particularly in Bute Inlet (mean resolution of 125 m instead of 251 m as in F12). The resulting grid exhibited a total of 39,532 nodes and 72,518 elements (Fig. Figure 11a). The model bathymetry was smoothed with a volume preserving technique that limits the ratio $\Delta h/h<0.1$ within each triangle in Bute and Toba Inlets; everywhere else, the threshold

70 was 0.3. The number of vertical terrain-following layers increased from 20 to 40, keeping higher resolution near the surface (surface layer represented 0.1% of the total water column; the coarser layer at the bottom represented 7.5% of the total depth). Only a few parameterizations and parameter values changed in the new version of the FVCOM Discovery Islands model with respect to F12. The new setup used the k-ε vertical turbulence closure scheme (Rodi, 1987) and a background vertical diffusion and viscosity of 10^{-5} m^2 s^{-1}. The remaining parameterizations and parameters stayed the same and most are listed here for

75 convenience. For instance, the Smagorinsky eddy parameterization was used for horizontal diffusivity with a coefficient C=0.02 and the horizontal viscosity was 10 times the diffusivity. Furthermore, the bottom roughness equation remained based on the General Ocean Turbulence Model (Burchard and Bolding, 2001) with a length scale of 10^{-3} m and a minimal value of 2.5 10^{-3} for the model bottom drag coefficient. The external and internal time steps were kept at 0.075 and 0.75 seconds (i.e., ISPLIT parameter set to 10). At the two open boundaries (one in the Johnstone Strait and the other in the Strait of Georgia,

80 Fig. 1a), implicit radiation conditions were used for temperature and salinity (Blumberg and Kantha, 1985) and clamped conditions for surface elevation (Beardsley and Haidvogel, 1981); moreover, a sponge layer of 7.5 km wide was set with a damping coefficient of 1.5 10^{-4}.

2.2 Model forcing and initialization

The external forcing and initialization changed substantially from the previous versions of this model. First of all, the time

85 period of simulation changed from April 2010 (F12) and April to October 2010 (Foreman et al., 2015) to May - June 2019, given the focus on understanding the stability of the subsurface temperature minimum found that year (Jackson et al., 2023). Furthermore, the present setup benefited from new operational models to force the boundaries of the FVCOM domain. At the surface, hourly forcing of winds, pressure, and heat and water fluxes were provided by the High Resolution Deterministic Prediction System (HRDPS). The first release of HRDPS offered a resolution of 2.5-km (Milbrandt et al., 2016), which was

90 suboptimal for a region with narrow inlets (~1 km wide) such as the Discovery Islands area; therefore, for this study we used the experimental HRDPS version at 1-km horizontal resolution (MSC Open Data, 2022). The SalishSeaCast model (Soontiens et al., 2016; Soontiens and Allen, 2017), a three-dimensional physical-biological-chemical ocean model for the Strait of Georgia and Salish Sea, provided hourly temperature, salinity and surface elevations for both the Johnstone Strait and Strait of Georgia open boundaries. Moreover, temperature and salinity fields from SalishSeaCast were used to initialize the FVCOM

95   simulation, except in Bute Inlet, where observed profiles from 23 May 2019 allowed for the best possible initialization of the subsurface temperature minimum.

The 11 rivers included in the model (Fig. 1a) were implemented analogously to F12, except that the temperature and salinity at the discharge nodes were calculated using a mass conservation approach rather than specifying the actual value (i.e. RIVER_TS_SETTING parameter was set to 'calculated' instead of 'specified'). Mean daily discharge values were acquired

100   from the Water Survey of Canada database for all available watersheds in and around the study area. As in the previous study, only four of the 11 rivers were gauged during 2019 (Homathko, Campbell, Salmon and Oyster Rivers) and for the seven ungauged rivers, a watershed area-ratio approach was used to estimate their discharge from representative donor gauges. In F12, all ungauged rivers were estimated as the Homathko River discharge multiplied by their watershed area ratio (i.e., area of ungauged river divided by area of Homathko River). However, the new version of the model took advantage of a recent

105   watershed characterization and classification (Giesbrecht et al., 2022) to select a representative donor gauge for each ungauged watershed. Specifically, each ungauged watershed was assigned a donor gauge from a nearby watershed of the same type (glacierized mountains or snow mountains) and with similar climate (e.g., mean annual precipitation and precipitation as snow) and hydrology (e.g., glacier cover, reservoirs, and regulated flows). Hence, while the Southgate and Toba Rivers still used the Homathko River (all three having a glacierized mountain watershed type), the Stafford, Apple, Phillips, and Brem Rivers based

110   their discharges on the Wakeman River (snow mountain watershed type). The Powell River was estimated from the Campbell River (gauge 08HD003, above the Quinsam River confluence), given that both are snow mountain type watersheds where discharge is controlled by dams (i.e., the underlying assumption being that both rivers were managed in the same way). For the Campbell River watershed, discharge was computed as the sum of flows from Campbell River above the Quinsam River confluence (gauge 08HD003) and Quinsam River near the same confluence (08HD005). Gauged discharges were scaled to

115   watershed-outlet discharges based on area ratios.

2.3 Model simulations and available observations

The model was run for ~1 month, from 24 May to 27 June 2019. The choice of this period was determined by several factors. First of all, observations from summer 2019 in Bute Inlet showed evidence of the subsurface temperature minimum (and oxygen maximum) generated the previous winter during an Arctic outflow wind event (Jackson et al., 2023). Observations in

120   Bute Inlet from 23 May (eight profiles) provided the temperature and salinity initial conditions in the fjord. Furthermore, HRDPS-1km outputs were available starting in 24 May 2019. The total length of the simulation allowed for 5 days of spinup and 29 days for analysis; the latter is an appropriate averaging period to remove tides and calculate residual flows (Foreman et al., 1992).

A sensitivity experiment was performed by removing the temperature minimum feature in Bute Inlet from the initial conditions.

125   In this simulation, initial temperature and salinity profiles in Bute Inlet were kept constant below the main pycnocline (Fig. A1); the constant values corresponded to the coolest and saltiest observations in the deepest third of the water column.

Available observations were mostly limited to vertical profiles, both from bottle and Conductivity-Temperature-Depth (CTD) measurements. In total, 114 profiles were available for the period 24 May - 27 June (see locations in Fig. 1b), representing 20,348 matches between modelled and observed temperatures (20,231 matches for salinity). Sea surface elevations were
130   available at the Campbell River tidal gauge (triangle in Fig. 1b).

2.4 Metrics for model evaluation

To evaluate the performance of the model, potential temperature (θ) and salinity fields were compared against observed values. For this purpose, model outputs were selected from the grid node closest to each observation and linearly interpolated in the vertical dimension and time to create model-observation pairs for each available in situ sample. With all the available pairs,
135   we calculated several metrics frequently used to quantify model-observations misfit. The model bias determines the mean deviation between modelled and observed values, while the root mean square error (RMSE) measures the deviation in a least-squares sense. These two metrics retain the units of the analysed variable. Two useful nondimensional metrics are the model efficiency (ME) or skill and the Willmott skill score (Willmott, 1981). The former relates the deviation between model and observations to the variability in the observations, while the latter is an indication of the model error divided by the range of
140   the observations. Both skill metrics can range from zero to one, with one indicating perfect agreement between observations and model. The latter is also the case for the square of the Pearson's correlation coefficient (R^2), which quantifies the correlation between modelled and observed data. A succinct but thorough description of these metrics can be found in Lehmann et al. (2009) and Liu et al. (2009).

3 Model evaluation

145   The model performance was evaluated through both quantitative and qualitative approaches. The quantitative metrics showed a good agreement between model and observations (Table 1). Biases were less than one tenth for both temperature and salinity (0.06 ℃ and 0.05 g kg^{-1}, respectively), while RMSEs were below 0.5 ℃ and 0.8 g kg^{-1}. All non-dimensional metrics were at or above 0.8, with particularly high Willmott skill scores of 0.95 and 0.93 for temperature and salinity, respectively. Metrics for sea surface height at Campbell River were also good, with bias and RMSE values of -16 and 21 cm, respectively, and non-
150   dimensional metrics above 0.95 (Table 1; Fig. A2).
Two-dimensional histograms (Fig. 2a and b) showed that most of the model-observations pairs fell right on top of the 1:1 slope for temperature and salinity. The least square linear fit (cyan line) for temperature had a slope of 0.9, quite close to the desired slope of one (Fig. 2a). For salinity, the spread at low observed values led to a less successful fit, with a slope of 0.6 (Fig. 2b). The model could not achieve the low salinities observed at surface in many inlets and channels with freshwater inputs, probably
155   due to numerical overmixing. Nevertheless, low salinity plumes were represented, albeit not reaching values as low as observed (see salinity profiles in Fig. 3). Furthermore, the model captured the statistical characteristics of the observations, shown by the overlap of model and observed histograms (Fig. 2c and d).

The model was able to represent the vertical structure of the observations in Bute Inlet (Fig. 3), which is the focus of this work. The observed temperature profiles showed a temperature minimum around 80 m depth, which was also present in the model

160 results (Fig. 3a, b). The modelled minimum was not as sharp as in the observations, likely due in part to numerical diffusion. As mentioned before, the model overestimated surface salinity (by several g kg^{-1}; Fig. 3c, d), leading also to an overestimation of surface density (Fig. 3e, f). Nevertheless, both the halocline and pycnocline were correctly represented by the model, with a sharp vertical gradient in the top 10 m of the water column. Bottom values were homogeneous and matched the observations below ~200 m.

4 Vertical structure of temperature and along inlet velocities

4.1 Baseline simulation with observed initial conditions

Temperature and along-inlet velocity were averaged over the last 29 days of the simulation. This averaging effectively filtered out the tides (to focus on residual flows) while also removed the first five days of simulation to allow for spin-up. A transect plot of mean along-inlet velocities through Bute Inlet showed a four-layered structure of the velocity field in most of the fjord

170 (Fig. 4a). The surface layer flowed outwards of the fjord, with a return flow immediately underneath, following a typical estuarine circulation. Below these two layers, there is a region of almost zero velocities at around 45 m deep. This region coincided with the location of the minimum averaged temperature along the inlet (Fig. 4b). Underneath, the averaged flow was into the inlet down to the depth of the outside sill (almost 300 m). Below the sill depth, the mean, slow flow was towards the mouth of the inlet.

175 To further explore the vertical structure of potential temperature and along-inlet velocity, profiles were plotted every 10 km in the middle of the inlet (from 20 to 50 km away from the head of the inlet; Fig. 5a to d). The four-layer structure is evident in the mean along-inlet velocity profiles, as well as the co-location of the temperature minimum feature and the zone with almost zero velocities. The minima in each profile is found between 44 and 46 m deep, with velocities ranging between -0.01 and -0.7 cm s^{-1} (negative values imply flow towards the head of the fjord).

4.2 Sensitivity simulation without temperature minimum feature

A sensitivity simulation with homogeneous conditions under the main pycnocline (as described in section 2.3) showed a three-layered circulation in the fjord (Fig. 4d and Fig. 5e to h), instead of the four layers found on the baseline simulation. The surface, outward-flowing layer was identical in both simulations (Fig. 4 and 5) and the bottom outward flow was quite similar (e.g., comparable magnitude, vertical distribution/shape, and depth range). However, the sensitivity experiment had a single

185 return flow between the surface layer and the depth of the sill with no near-zero flow in the upper 100 m. Additional sensitivity simulations (not shown), indicated that salinity was the crucial variable at determining whether the circulation was three- or four-layered (i.e., if only temperature was homogenized below the pycnocline in the initial conditions, the residual circulation was not clearly three-layered).

The cold subsurface feature can be identified as a new water mass when comparing temperature-salinity diagrams for both the
190   baseline and sensitivity simulations (Fig. 6a; only model values at the time and location of the observations were plotted to
simplify the figure). The strong winter mixing event not only led to subsurface cooling and reoxygenation, but also affected
salinity and led to density and stratification changes (Fig. 6b, c). In particular, stratification decreased below the outward-
flowing layer (Fig. 6c) and density increased in that same region (Fig. 6b). These changes were not uniform in the horizontal,
but stronger near the head of the inlet; given the overall horizontal density gradient near the surface (lower density near the
195   head due to the freshwater inputs), the subsurface water mass led to a reduced horizontal density difference between the head
and the mouth of Bute Inlet.

5 Discussion

The modelled circulation in Bute Inlet, as observed in many other fjords, is estuarine and multi-layered (e.g., Baker & Pond,
1995; Stacey & Gratton, 2001; Valle-Levinson et al., 2007, 2014; Wan et al., 2017). The overall summer residual circulation
200   in the deep Bute Inlet was relatively slow, with time-averaged flows below the surface under 5 cm s^{-1} (Figs. 4 and 5); these
values are comparable with some fjords, e.g. Reloncavi fjord in Chile (Valle-Levinson et al., 2007, 2014) and Knight Inlet in
BC (Baker and Pond, 1995), but lower than many others that easily exceed 10 cm s^{-1} (e.g., Stacey and Gratton, 2001; Valle-
Levinson et al., 2014; Wan et al., 2017; Jackson and Straneo, 2016). In particular, the mean residual three-layer structure found
in Bute Inlet in the absence of the cold subsurface water mass (Figs. 4d, e and 5e to h) was consistent with the expectations for
205   such a deep fjord, following Valle-Levinson et al. (2014) and references therein. These authors discussed the application of
theoretical work on tidally forced narrow channels with flat or simplified bathymetry (Ianniello, 1977; Winant, 2008) to
describe one-, two-, and three-layered flows in fjords. The layering of the circulation depends on the value of δ, the inverse of
the Stokes number ($\delta = \sqrt{\omega H^2 / A_z}$, where ω is the frequency of tidal forcing, H is the depth of the channel, and A_z is the
vertical eddy viscosity). For channels with δ ≤ 2, the residual Eulerian flow is seaward throughout the water column. For 3 ≤
210   δ ≤ 5, a two-layered residual flow has inflow at the surface and outflow underneath. A three-layered residual flow structure
occurs for values of δ ≥ 6 (outflow at the surface and bottom, with inflow in between). In other words, Valle-Levinson et al.
(2014) described δ as a dynamical depth of the system that compares the total water column depth against the depth of frictional
influence in an oscillatory flow. In deep fjords (as it is the case of Bute Inlet), the frictional depth represents only a small
portion of the water column and the tidal residual flow is expected to be three-layered. Using representative values for Bute
215   Inlet from the model (mean H = 500 m, mean A_z = 4 10^{-4} m^2 s^{-1}, and ω = 1.4 10^{-4} rad s^{-1} for the dominant tidal constituent,
M2), the resulting δ = 296 is indeed consistent with a three-layer structure.

However, the presence of the temperature minimum feature created a separation of the return flow, such that velocities
remained close to zero at the core of the temperature minimum (Figs. 4a, b and 5a to d). Furthermore, the overall along-inlet
velocities were weaker in the baseline simulation compared with the sensitivity case (Figs. 4a, d and 5). The temperature
220   minimum originated during the previous winter, when a strong Arctic wind outflow event over Bute Inlet vertically mixed the

top ~100 m of the water column, leading to cooling and oxygenation down to that depth (Jackson et al., 2023). This deep winter mixing created a new water mass, since not only temperature and oxygen, but also salinity and density were impacted; as the surface conditions changed along with the seasons (surface warming in spring/summer as well as freshening due to summer river freshet), the new cold water mass became isolated from the surface and remained constrained to the subsurface

225   (at ~ 80 m depth; Fig. 4b). The cold water mass led to less stratification (Fig. 6c), allowing for more mixing of dense water into the upper layers, particularly closer to the head of the inlet (Fig. 6b). The latter led to a reduced density difference along the fjord near the surface, effectively reducing the strength of the estuarine circulation and decreasing the along-inlet mean velocities. The weaker velocities overall decreased mixing and advection, allowing for the cold water mass to remain in place until the arrival of strong autumn/winter wind-driven deep mixing.

230   Model and observational studies have previously found multi-layer structures of the mean residual flow in fjords around the globe. While many regions present typical estuarine two-layer structures (e.g., Khangaonkar et al., 2011; Sciascia et al., 2013; Stigebrandt, 1981), many others exhibit more complex structures (e.g., Baker & Pond, 1995; Stacey & Gratton, 2001; Valle-Levinson et al., 2007, 2014; Wan et al., 2017). Valle-Levinson (2014) highlighted the difficulty in observing the multi-layer residual structure, since it is easily masked by the many acting forces at play in the nearshore (e.g., wind forcing, remote

235   forcing from the ocean, freshwater inputs). Timeseries of moored instruments are required to observe the vertical structure of residual flows, which can also change with seasons (Wan et al., 2017) and between years (Baker and Pond, 1995). Model simulations like the one presented here are also useful tools to explore fjord circulation under different conditions, particularly allowing one to disentangle the mechanisms at play.

6 Summary and conclusions

240   Here we described how a deep, narrow fjord such as Bute Inlet responds to a three-layer circulation pattern under standard summer conditions, consistent with theoretical arguments (Ianniello, 1977; Valle-Levinson et al., 2014). Outflow occurs at surface and depth, with inflow into the inlet in-between those two layers. However, when a new water mass is created in winter during a strong mixing event, the detided circulation turns into a four-layer structure in the vertical, with the incoming flow finding its way above and below the winter-formed water mass. Averaged four-layer flows were observed in other systems

245   and linked to other physical processes; for instance, the coupling between deep water renewal and estuarine circulation through conservation of volume explained multi-layers in other fjords in British Columbia (Baker and Pond, 1995; Wan et al., 2017). Our study highlights how a fjord's circulation can be changed for the whole year by an extreme wind mixing event in winter. Furthermore, in the context of climate change, with globally observed oxygen declines and warming temperatures in fjords (e.g., Aksnes et al., 2019; Jackson et al., 2021; Linford et al., 2023), mechanisms that allow for the persistence of cold and

250   oxygenated waters could alleviate the negative consequences of global warming and potentially create temporal ecological refugia.

Appendix A

Profiles of initial conditions in a mid-inlet station ('BU4' at 50.6ºN and 124.9ºW) help further describe the difference between the baseline and sensitivity simulations (Fig. A1). The figure also shows the observations from 23 May 2019 that were used

255 to create the baseline initial conditions. Lastly, the comparison between modelled and observed time series of surface elevation at the Campbell River tidal gauge provide an additional visualization of the evaluation of model performance (Fig. A2).

Code availability

FVCOM code is publicly available by their developers at https://github.com/FVCOM-GitHub/FVCOM.

Data availability

260 Ocean observations used in this manuscript can be found in the publicly available Canadian Integrated Ocean Observing System repository (https://www.cioos.ca/). River discharge data are publicly available through the Water Survey of Canada (https://wateroffice.ec.gc.ca/). Furthermore, both model and observational datasets will be uploaded to the Canadian Open Government Portal upon acceptance of the manuscript. Only model outputs used in the figures will be uploaded given the large size of the model output files. Further model data would be available upon request.

Author contribution

265 LB conceptualized the project, obtained funding, performed model simulations and analysis, produced the figures, wrote the original draft, and led the manuscript to its final form. All co-authors participated in the review and editing of the original draft. JMJ and SEA contributed to the analysis and interpretation of model results. MK developed the modifications to the model grid in Bute and Toba Inlets. IJWG improved the methods to estimate river discharge for ungauged rivers and provided

270 the related data.

Competing interests

The authors declare that they have no conflict of interest.

Acknowledgments

This work was funded by Fisheries and Oceans Canada partly through the Program in Aquaculture Regulatory Research. The
275 authors are grateful to members of the UBC-DFO Modelling Working Group for many useful discussions and suggestions during our group meetings, including (but not limited to) Mike Foreman, Michael Dunphy, Amber Holdsworth, and Di Wan.

Hayley Dosser, Shani Rousseau, Peter Chandler, and Pramod Thupaki provided support at early stages of this work. Di Wan provided an internal DFO review before submission. We gratefully acknowledge that ocean sampling in this work took place on the traditional territories of the Homalco and other First Nations.

References

Aksnes, D. L., Aure, J., Johansen, P.-O., Johnsen, G. H., and Vea Salvanes, A. G.: Multi-decadal warming of Atlantic water and associated decline of dissolved oxygen in a deep fjord, Estuarine, Coastal and Shelf Science, 228, 106392, https://doi.org/10.1016/j.ecss.2019.106392, 2019.

Government of Canada: https://open.canada.ca/data/en/dataset/e6e11b99-f0cc-44f7-f5eb-3b995fb1637e, last access: 7 July 2021.

Arimitsu, M. L., Piatt, J. F., Madison, E. N., Conaway, J. S., and Hillgruber, N.: Oceanographic gradients and seabird prey community dynamics in glacial fjords: Glacial fjord marine habitat, Fisheries Oceanography, 21, 148–169, https://doi.org/10.1111/j.1365-2419.2012.00616.x, 2012.

Bailey, L. P., Clare, M. A., Pope, E. L., Haigh, I. D., Cartigny, M. J. B., Talling, P. J., Lintern, D. G., Hage, S., and Heijnen, M.: Predicting turbidity current activity offshore from meltwater-fed river deltas, Earth and Planetary Science Letters, 604, 117977, https://doi.org/10.1016/j.epsl.2022.117977, 2023.

Baker, P. and Pond, S.: The Low-Frequency Residual Circulation in Knight Inlet, British Columbia, J. Phys. Oceanogr., 25, 747–763, https://doi.org/10.1175/1520-0485(1995)025<0747:TLFRCI>2.0.CO;2, 1995.

Ball, A. M.: Fisheries at a new scale: The contributions of archaeological fish scales in understanding Indigenous fisheries in Wuikinuxv First Nation territory and beyond, University of Victoria, Victoria, BC, 146+xiii pp., 2021.

Beardsley, R. C. and Haidvogel, D. B.: Model Studies of the Wind-Driven Transient Circulation in the Middle Atlantic Bight. Part 1: Adiabatic Boundary Conditions, J. Phys. Oceanogr., 11, 355–375, https://doi.org/10.1175/1520-0485(1981)011<0355:MSOTWD>2.0.CO;2, 1981.

Bergh, Ø., Beck, A. C., Tassetti, A. N., Olsen, E., Thangstad, T. H., Gonzalez-Mirelis, G., Grati, F., Bolognini, L., and Søvik, G.: Analysis of spatial conflicts of large scale salmonid aquaculture with coastal fisheries and other interests in a Norwegian fjord environment, using the novel GIS-tool SEAGRID and stakeholder surveys, Aquaculture, 574, 739643, https://doi.org/10.1016/j.aquaculture.2023.739643, 2023.

Bianchi, T. S., Arndt, S., Austin, W. E. N., Benn, D. I., Bertrand, S., Cui, X., Faust, J. C., Koziorowska-Makuch, K., Moy, C. M., Savage, C., Smeaton, C., Smith, R. W., and Syvitski, J.: Fjords as Aquatic Critical Zones (ACZs), Earth-Science Reviews, 203, 103145, https://doi.org/10.1016/j.earscirev.2020.103145, 2020.

Blumberg, A. F. and Kantha, L. H.: Open Boundary Condition for Circulation Models, J. Hydraul. Eng., 111, 237–255, https://doi.org/10.1061/(ASCE)0733-9429(1985)111:2(237), 1985.

Brattland, C.: Mapping Rights in Coastal Sami Seascapes, Arctic Review on Law and Politics, 1, 28–53, 2010.

Burchard, H. and Bolding, K.: Comparative Analysis of Four Second-Moment Turbulence Closure Models for the Oceanic
310   Mixed Layer, J. Phys. Oceanogr., 31, 1943–1968, https://doi.org/10.1175/1520-0485(2001)031<1943:CAOFSM>2.0.CO;2,
2001.

Chen, C., Liu, H., and Beardsley, R. C.: An Unstructured Grid, Finite-Volume, Three-Dimensional, Primitive Equations Ocean
Model: Application to Coastal Ocean and Estuaries, J. Atmos. Oceanic Technol., 20, 159–186, https://doi.org/10.1175/1520-
0426(2003)020<0159:AUGFVT>2.0.CO;2, 2003.

315   Chen, C., Beardsley, R., and Cowles, G.: An Unstructured Grid, Finite-Volume Coastal Ocean Model (FVCOM) System,
Oceanog., 19, 78–89, https://doi.org/10.5670/oceanog.2006.92, 2006.

Chen, C., Beardsley, R. C., Cowles, G., Qi, J., Lai, Z., Gao, G., Stuebe, D., Liu, H., Xu, Q., Xue, P., Ge, J., Hu, S., Ji, R., Tian,
R., Huang, H., Wu, L., Lin, H., Sun, Y., and Zhao, L.: An unstructured grid, finite-volume community ocean model. FVCOM
user manual, University of Massachusetts-Dartmouth, 2013.

320   Ducklow, H., Cimino, M., Dunton, K. H., Fraser, W. R., Hopcroft, R. R., Ji, R., Miller, A. J., Ohman, M. D., and Sosik, H.
M.: Marine Pelagic Ecosystem Responses to Climate Variability and Change, BioScience, 72, 827–850,
https://doi.org/10.1093/biosci/biac050, 2022.

MSC Open Data: https://eccc-msc.github.io/open-data/msc-data/nwp_hrdps/readme_hrdps-datamart-alpha_en/, last access:
26 August 2022.

325   Farrow, G. E., Syvitski, J. P. M., and Tunnicliffe, V.: Suspended Particulate Loading on the Macrobenthos in a Highly Turbid
Fjord: Knight Inlet, British Columbia, Can. J. Fish. Aquat. Sci., 40, s273–s288, https://doi.org/10.1139/f83-289, 1983.

Foreman, M. G. G., Baptista, A. M., and Walters, R. A.: Tidal model studies of particle trajectories around a shallow coastal
bank, Atmosphere-Ocean, 30, 43–69, https://doi.org/10.1080/07055900.1992.9649430, 1992.

Foreman, M. G. G., Stucchi, D. J., Garver, K. A., Tuele, D., Isaac, J., Grime, T., Guo, M., and Morrison, J.: A Circulation
330   Model   for   the   Discovery   Islands,   British   Columbia,   Atmosphere-Ocean,   50,   301–316,
https://doi.org/10.1080/07055900.2012.686900, 2012.

Foreman, M. G. G., Guo, M., Garver, K. A., Stucchi, D., Chandler, P., Wan, D., Morrison, J., and Tuele, D.: Modelling
Infectious Hematopoietic Necrosis Virus Dispersion from Marine Salmon Farms in the Discovery Islands, British Columbia,
Canada, PLoS ONE, 10, e0130951, https://doi.org/10.1371/journal.pone.0130951, 2015.

335   Frid, A., McGreer, M., Wilson, K. L., Du Preez, C., Blaine, T., and Norgard, T.: Hotspots for rockfishes, structural corals, and
large-bodied sponges along the central coast of Pacific Canada, Sci Rep, 11, 21944, https://doi.org/10.1038/s41598-021-
00791-9, 2021.

Geertsema, M., Menounos, B., Bullard, G., Carrivick, J. L., Clague, J. J., Dai, C., Donati, D., Ekstrom, G., Jackson, J. M.,
Lynett, P., Pichierri, M., Pon, A., Shugar, D. H., Stead, D., Del Bel Belluz, J., Friele, P., Giesbrecht, I., Heathfield, D., Millard,
340   T., Nasonova, S., Schaeffer, A. J., Ward, B. C., Blaney, D., Blaney, E., Brillon, C., Bunn, C., Floyd, W., Higman, B., Hughes,
K. E., McInnes, W., Mukherjee, K., and Sharp, M. A.: The 28 November 2020 Landslide, Tsunami, and Outburst Flood – A
Hazard Cascade Associated With Rapid Deglaciation at Elliot Creek, British Columbia, Canada, Geophysical Research Letters,
49, e2021GL096716, https://doi.org/10.1029/2021GL096716, 2022.

Giesbrecht, I. J. W., Tank, S. E., Frazer, G. W., Hood, E., Gonzalez Arriola, S. G., Butman, D. E., D'Amore, D. V., Hutchinson,
345   D., Bidlack, A., and Lertzman, K. P.: Watershed Classification Predicts Streamflow Regime and Organic Carbon Dynamics

in the Northeast Pacific Coastal Temperate Rainforest, Global Biogeochemical Cycles, 36, https://doi.org/10.1029/2021GB007047, 2022.

Hage, S., Galy, V. V., Cartigny, M. J. B., Heerema, C., Heijnen, M. S., Acikalin, S., Clare, M. A., Giesbrecht, I., Gröcke, D. R., Hendry, A., Hilton, R. G., Hubbard, S. M., Hunt, J. E., Lintern, D. G., McGhee, C., Parsons, D. R., Pope, E. L., Stacey, C.
350 D., Sumner, E. J., Tank, S., and Talling, P. J.: Turbidity Currents Can Dictate Organic Carbon Fluxes Across River-Fed Fjords: An Example From Bute Inlet (BC, Canada), JGR Biogeosciences, 127, e2022JG006824, https://doi.org/10.1029/2022JG006824, 2022.

Heijnen, M. S., Clare, M. A., Cartigny, M. J. B., Talling, P. J., Hage, S., Lintern, D. G., Stacey, C., Parsons, D. R., Simmons, S. M., Chen, Y., Sumner, E. J., Dix, J. K., and Hughes Clarke, J. E.: Rapidly-migrating and internally-generated knickpoints
355 can control submarine channel evolution, Nat Commun, 11, 3129, https://doi.org/10.1038/s41467-020-16861-x, 2020.

Ianniello, J. P.: Tidally induced residual currents in estuaries of constant breadth and depth, Journal of Marine Research, 35, 755–785, 1977.

Iriarte, J. L., González, H. E., and Nahuelhual, L.: Patagonian Fjord Ecosystems in Southern Chile as a Highly Vulnerable Region: Problems and Needs, AMBIO, 39, 463–466, https://doi.org/10.1007/s13280-010-0049-9, 2010.

360 Jackson, J. M., Bianucci, L., Hannah, C. G., Carmack, E. C., and Barrette, J.: Deep Waters in British Columbia Mainland Fjords Show Rapid Warming and Deoxygenation From 1951 to 2020, Geophysical Research Letters, 48, https://doi.org/10.1029/2020GL091094, 2021.

Jackson, J. M., Holmes, K., Klymak, J. M., Bianucci, L., Evans, W., Floyd, W. C., Hannah, C. G., Hare, A., and Wan, D.: Winter Arctic Outflow Winds Cause Upper Ocean Cooling and Reoxygenation in a Temperate Canadian Fjord, Geophysical
365 Research Letters, 50, e2023GL104549, https://doi.org/10.1029/2023GL104549, 2023.

Jackson, R. H. and Straneo, F.: Heat, Salt, and Freshwater Budgets for a Glacial Fjord in Greenland, Journal of Physical Oceanography, 46, 2735–2768, https://doi.org/10.1175/JPO-D-15-0134.1, 2016.

Keen, E., Wray, J., Meuter, H., Thompson, K., Barlow, J., and Picard, C.: 'Whale wave': shifting strategies structure the complex use of critical fjord habitat by humpbacks, Mar. Ecol. Prog. Ser., 567, 211–233, https://doi.org/10.3354/meps12012,
370 2017.

Khangaonkar, T., Yang, Z., Kim, T., and Roberts, M.: Tidally averaged circulation in Puget Sound sub-basins: Comparison of historical data, analytical model, and numerical model, Estuarine, Coastal and Shelf Science, 93, 305–319, https://doi.org/10.1016/j.ecss.2011.04.016, 2011.

Lehmann, M. K., Fennel, K., and He, R.: Statistical validation of a 3-D bio-physical model of the western North Atlantic,
375 Biogeosciences, 6, 1961–1974, https://doi.org/10.5194/bg-6-1961-2009, 2009.

Linford, P., Pérez-Santos, I., Montes, I., Dewitte, B., Buchan, S., Narváez, D., Saldías, G., Pinilla, E., Garreaud, R., Díaz, P., Schwerter, C., Montero, P., Rodríguez-Villegas, C., Cáceres-Soto, M., Mancilla-Gutiérrez, G., and Altamirano, R.: Recent Deoxygenation of Patagonian Fjord Subsurface Waters Connected to the Peru–Chile Undercurrent and Equatorial Subsurface Water Variability, Global Biogeochemical Cycles, 37, e2022GB007688, https://doi.org/10.1029/2022GB007688, 2023.

380 Liu, Y., MacCready, P., Hickey, B. M., Dever, E. P., Kosro, P. M., and Banas, N. S.: Evaluation of a coastal ocean circulation model for the Columbia River plume in summer 2004, J. Geophys. Res., 114, C00B04, https://doi.org/10.1029/2008JC004929, 2009.

MacNeill, M. T.: The mid-depth temperature minimum in B.C. inlets, Master of Science, The University of British Columbia, Vancovuer, BC, 91+viii pp., 1974.

385 Mathews, E. A. and Pendleton, G. W.: Declines in harbor seal (phoca vitulina) numbers in Glacier Bay National Park, Alaska, 1992-2002, Marine Mammal Science, 22, 167–189, https://doi.org/10.1111/j.1748-7692.2006.00011.x, 2006.

Milbrandt, J. A., Bélair, S., Faucher, M., Vallée, M., Carrera, M. L., and Glazer, A.: The Pan-Canadian High Resolution (2.5 km) Deterministic Prediction System, Weather and Forecasting, 31, 1791–1816, https://doi.org/10.1175/WAF-D-16-0035.1, 2016.

390 Pickard, G. L.: Oceanographic Features of Inlets in the British Columbia Mainland Coast, J. Fish. Res. Bd. Can., 18, 907–999, https://doi.org/10.1139/f61-062, 1961.

Rodi, W.: Examples of calculation methods for flow and mixing in stratified fluids, J. Geophys. Res., 92, 5305, https://doi.org/10.1029/JC092iC05p05305, 1987.

Sciascia, R., Straneo, F., Cenedese, C., and Heimbach, P.: Seasonal variability of submarine melt rate and circulation in an
395 East Greenland fjord: FJORD DYNAMICS AND SUBMARINE MELTING, J. Geophys. Res. Oceans, 118, 2492–2506, https://doi.org/10.1002/jgrc.20142, 2013.

Smith, R. W., Bianchi, T. S., Allison, M., Savage, C., and Galy, V.: High rates of organic carbon burial in fjord sediments globally, Nature Geosci, 8, 450–453, https://doi.org/10.1038/ngeo2421, 2015.

Soontiens, N. and Allen, S. E.: Modelling sensitivities to mixing and advection in a sill-basin estuarine system, Ocean
400 Modelling, 112, 17–32, https://doi.org/10.1016/j.ocemod.2017.02.008, 2017.

Soontiens, N., Allen, S. E., Latornell, D., Le Souëf, K., Machuca, I., Paquin, J.-P., Lu, Y., Thompson, K., and Korabel, V.: Storm Surges in the Strait of Georgia Simulated with a Regional Model, Atmosphere-Ocean, 54, 1–21, https://doi.org/10.1080/07055900.2015.1108899, 2016.

St. Pierre, K. A., Hunt, B. P. V., Giesbrecht, I. J. W., Tank, S. E., Lertzman, K. P., Del Bel Belluz, J., Hessing-Lewis, M. L.,
405 Olson, A., and Froese, T.: Seasonally and Spatially Variable Organic Matter Contributions From Watershed, Marine Macrophyte, and Pelagic Sources to the Northeast Pacific Coastal Ocean Margin, Front. Mar. Sci., 9, 863209, https://doi.org/10.3389/fmars.2022.863209, 2022.

Stacey, M. W. and Gratton, Y.: The Energetics and Tidally Induced Reverse Renewal in a Two-Silled Fjord, J. Phys. Oceanogr., 31, 1599–1615, https://doi.org/10.1175/1520-0485(2001)031<1599:TEATIR>2.0.CO;2, 2001.

410 Stigebrandt, A.: A mechanism governing the estuarine circulation in deep, strongly stratified fjords, Estuarine, Coastal and Shelf Science, 13, 197–211, https://doi.org/10.1016/S0302-3524(81)80076-X, 1981.

Valle-Levinson, A., Sarkar, N., Sanay, R., Soto, D., and León, J.: Spatial structure of hydrography and flow in a Chilean fjord, Estuario Reloncaví, Estuaries and Coasts, 30, 113–126, https://doi.org/10.1007/BF02782972, 2007.

Valle-Levinson, A., Caceres, M. A., and Pizarro, O.: Variations of tidally driven three-layer residual circulation in fjords,
415 Ocean Dynamics, 64, 459–469, https://doi.org/10.1007/s10236-014-0694-9, 2014.

Wan, D., Hannah, C. G., Foreman, M. G. G., and Dosso, S.: Subtidal circulation in a deep-silled fjord: Douglas Channel, British Columbia: SUBTIDAL CIRCULATION IN DOUGLAS CHANNEL, J. Geophys. Res. Oceans, 122, 4163–4182, https://doi.org/10.1002/2016JC012022, 2017.

Willmott, C. J.: On the validation of models, Physical Geography, 2, 184–194,
420 https://doi.org/10.1080/02723646.1981.10642213, 1981.

Winant, C. D.: Three-Dimensional Residual Tidal Circulation in an Elongated, Rotating Basin, Journal of Physical Oceanography, 38, 1278–1295, https://doi.org/10.1175/2007JPO3819.1, 2008.
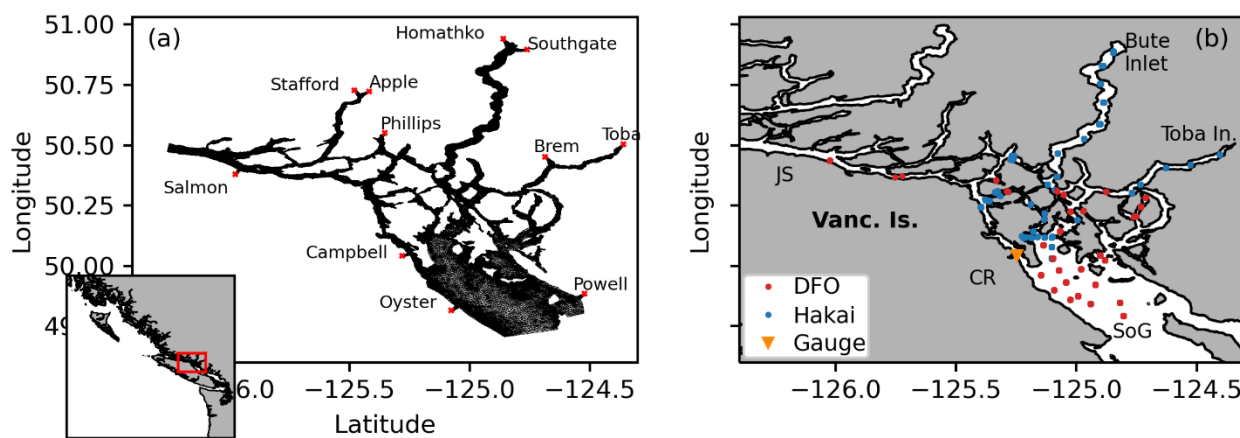
425 **Figure 1: (a) Model grid and location of rivers used to force the model; the red box in the inset shows the domain location on the west coast of Canada. Note that the model grid has such high resolution that it mostly shows as black. (b) Location of the observations for the period of study, colour coded by source (Fisheries and Oceans Canada/DFO and Hakai Institute); the triangle depicts the location of the Campbell River tidal gauge. Geographical places mentioned in the text are shown: Bute Inlet, Toba Inlet, Strait of Georgia (SoG), Johnstone Strait (JS), Campbell River (CR) and Vancouver Island.**
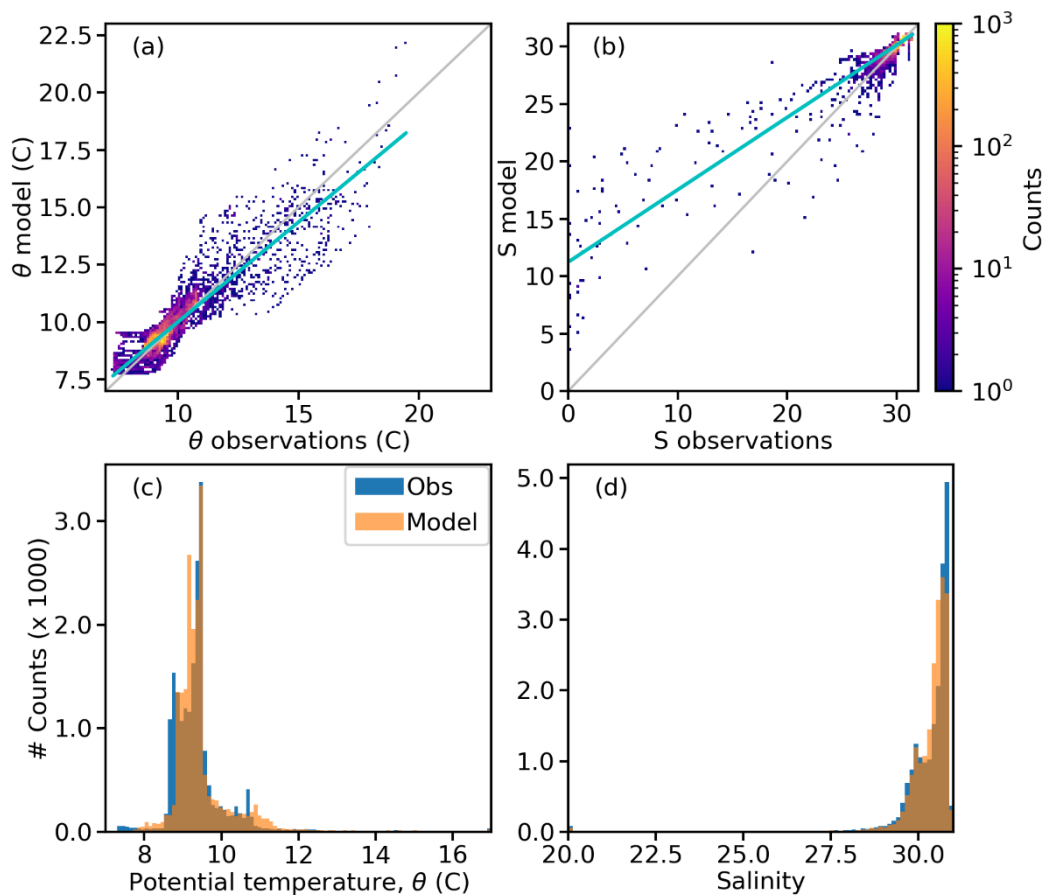
Figure 2. Two-dimensional histograms for (a) potential temperature and (b) salinity; the gray line shows the 1:1 slope and the cyan line, the linear regression fit. Overlapped model and observed histograms for (c) potential temperature and (d) salinity.
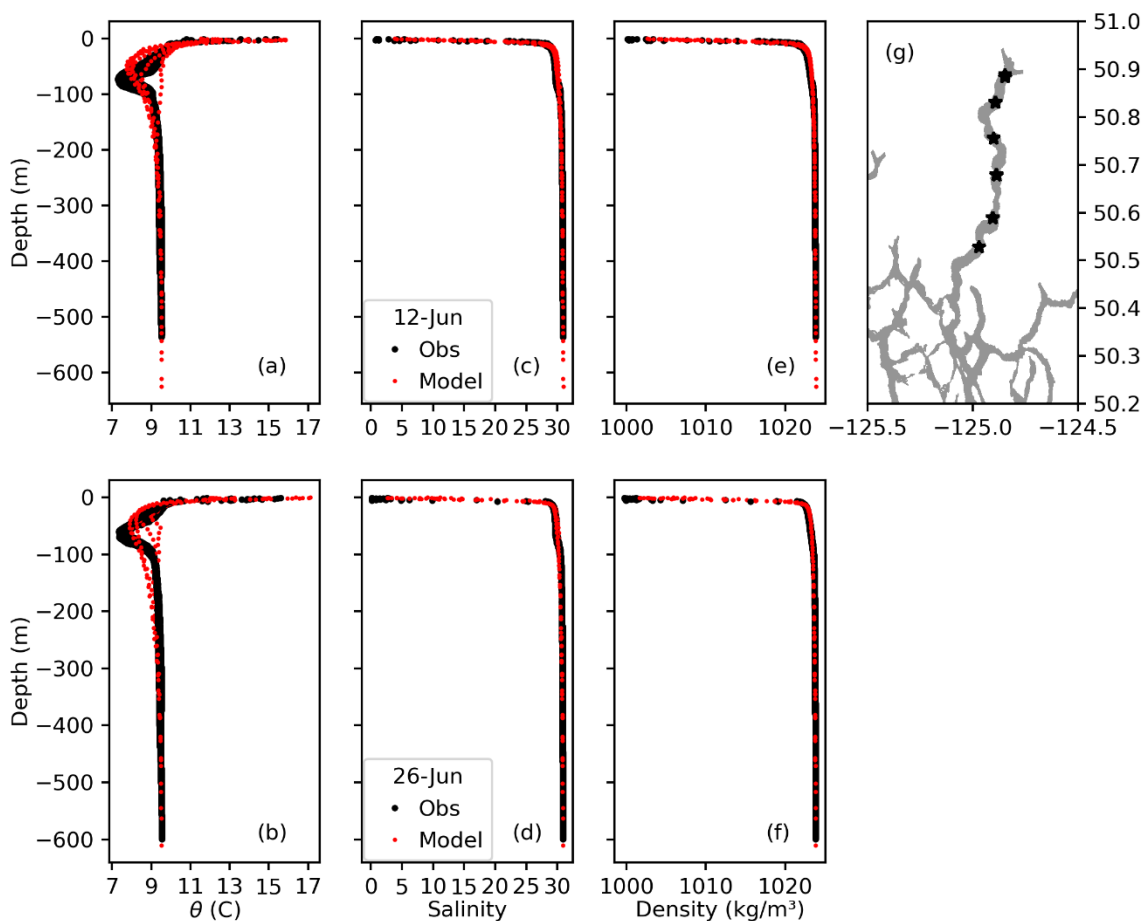
Figure 3. Comparison of modeled (red) vs. observed (black) profiles in Bute Inlet. Each row shows profiles for a given date (12 and 26 June 2019). Variables shown are (a, b) potential temperature, (c, d) salinity, and (e, f) density. (g) Locations of the profiles in Bute Inlet.
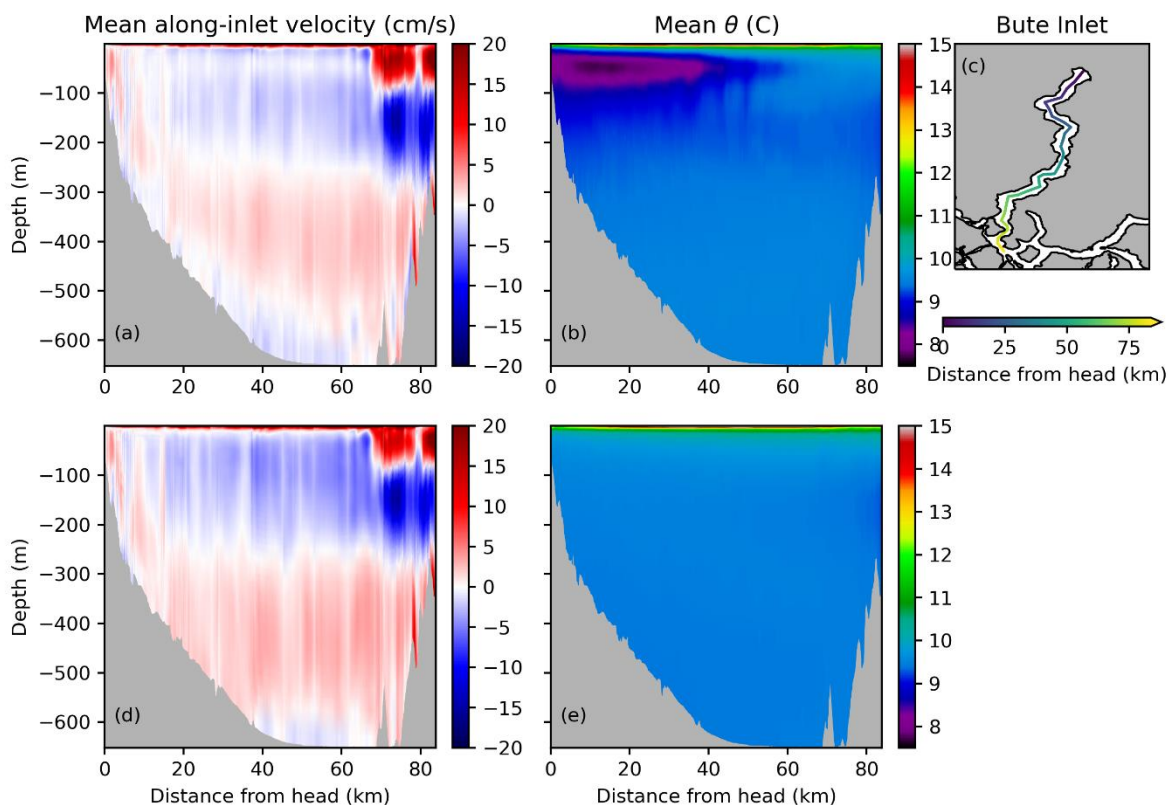
Figure 4. Mean along-inlet transects throughout Bute Inlet for (a, b) baseline and (d, e) sensitivity simulations. Variables shown are (a, d) mean along inlet velocity and (b, e) mean potential temperature. Velocities are positive (red) towards the mouth of the inlet and negative (blue) towards the head. Averages over the last 29 days of the simulation removed tidal effects. (c) Map of Bute Inlet transect, color-coded by the distance from the head of the inlet.

440
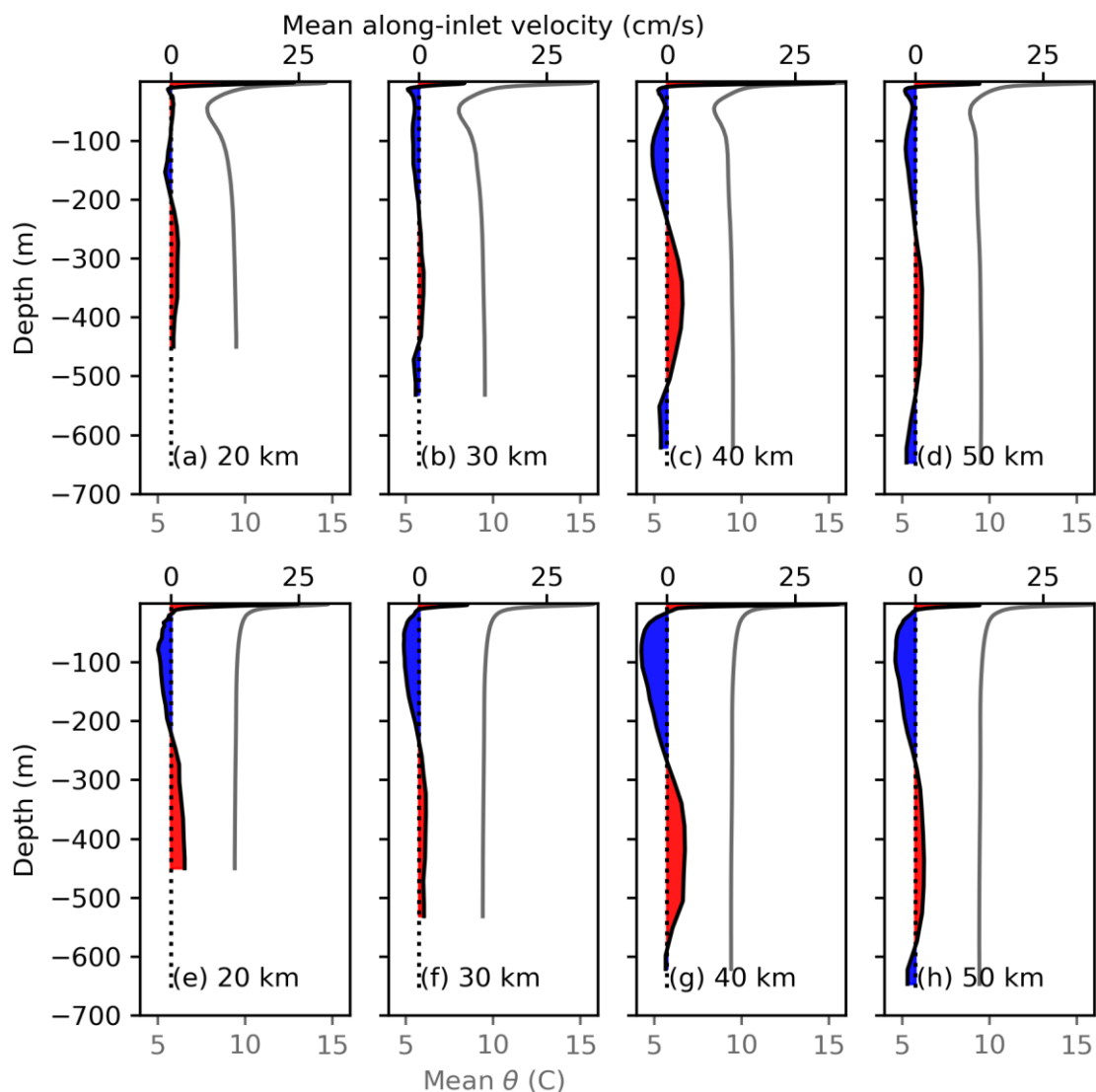
Figure 5. Vertical profiles of mean along-inlet velocity (colored red/blue) and potential temperature (grey) for the (a-d) baseline and (e-h) sensitivity simulations, at four locations in the inlet (from left to right: 20, 30, 40, and 50 km away from the head; see Fig. 4c). Velocities are positive (red) towards the mouth of the inlet and negative (blue) towards the head.
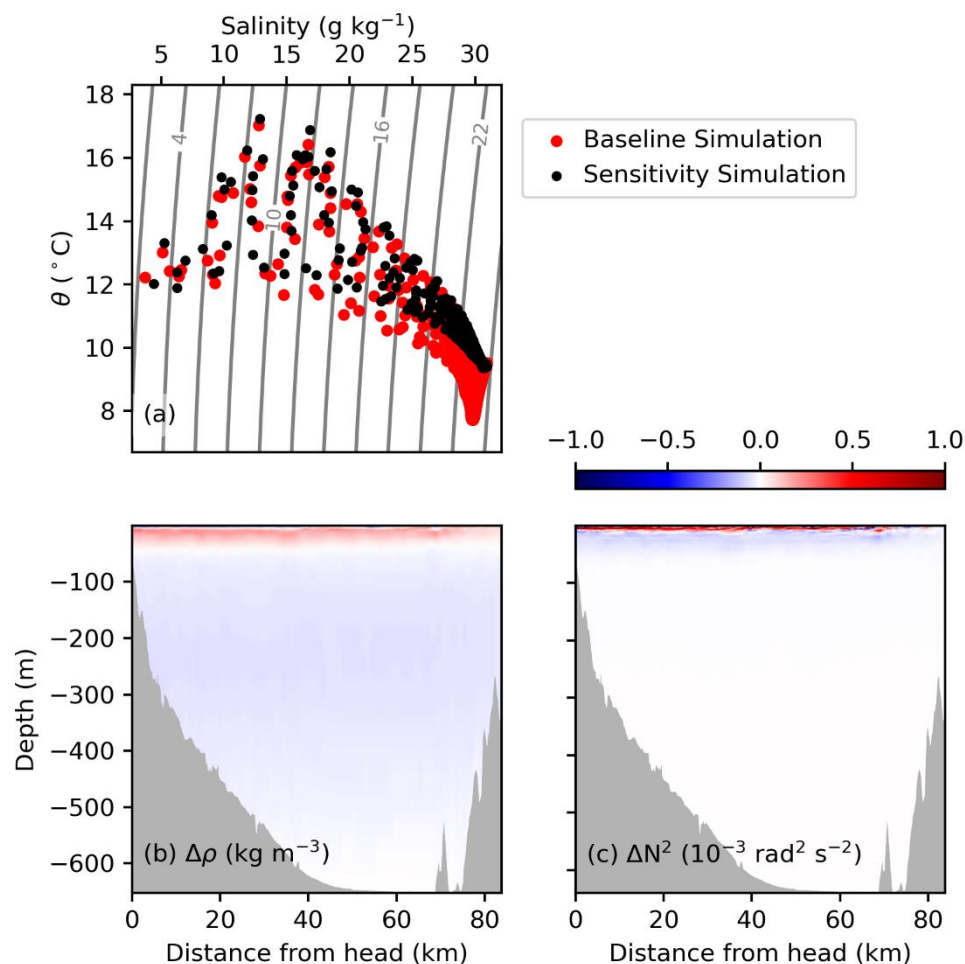
Figure 6. (a) Temperature-salinity diagram for the baseline (red) and sensitivity (black) simulations in Bute Inlet. Model results shown at the time and location of the observations (12 and 26 June 2019; location in Fig. 4g); for reference, four isopycnals were labeled according to their σ_θ (kg m⁻³). Bottom panels show along-inlet transects of the difference in (b) mean density and (c) mean Brunt-Väisälä frequency (N²) between baseline and sensitivity experiments (Δ = 29-day average baseline minus 29-day average sensitivity; negative values indicate that the baseline is less dense/stratified than the sensitivity simulation).

450

Table 1. Metrics calculated to compare model performance against observations.

Metric	Potential temperature, θ	Salinity	Sea level
Bias	0.08 ℃	0.05 g kg⁻¹	-16 cm
RMSE	0.44 ℃	0.73 g kg⁻¹	21 cm
Skill	0.81	0.80	0.95
Willmott skill	0.95	0.93	0.99
R^2	0.82	0.87	0.98
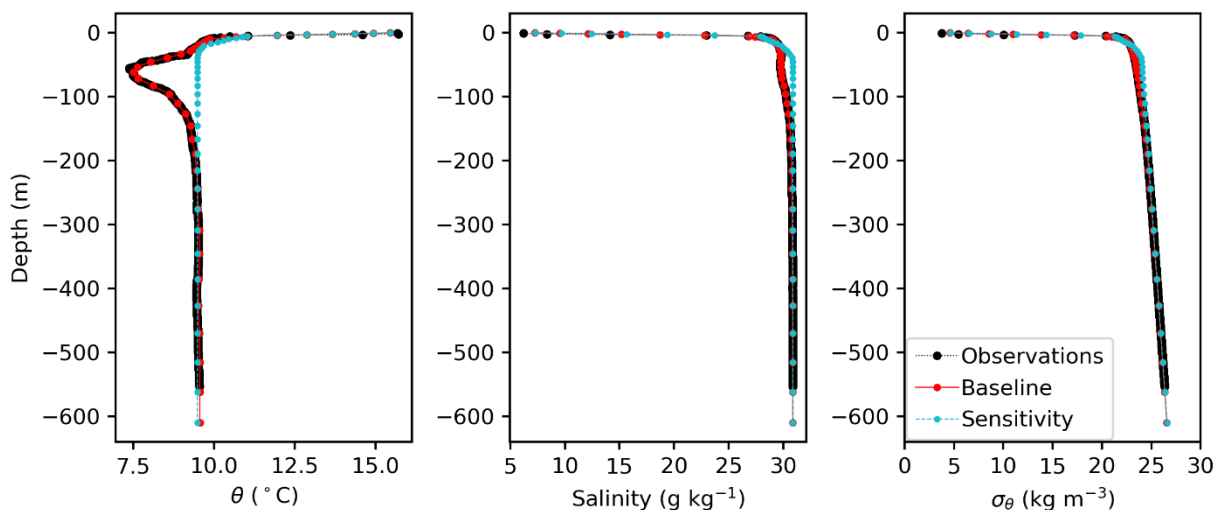
Figure A1. Profiles of potential temperature, salinity, and density (as σ_θ) at station BU4 (middle of the inlet at 50.6ºN and 124.9ºW) for the observations on 23 May 2019 (black) and the initial conditions for the baseline (red) and sensitivity (blue) simulations.
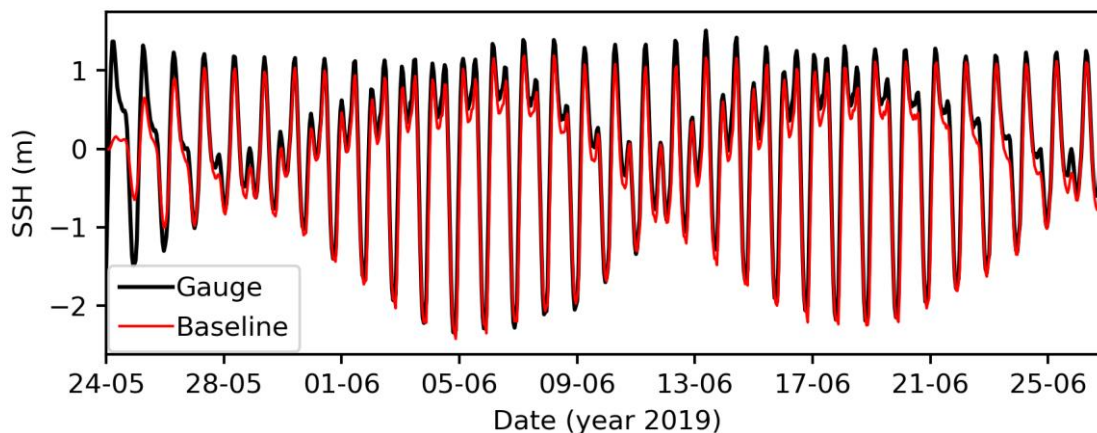
Figure A2. Observed (black) and modelled (red) time series of sea surface height (SSH) at Campbell River. Location of tidal gauge shown as a triangle in Fig. 1b.

460